

WIDE OPERATING RANGE FOR A CIRCULAR WAVEGUIDE PROBE IN  
SPHERICAL NEAR-FIELD MEASUREMENTS

---

A Thesis  
Presented to  
the Graduate School of  
Clemson University

---

In Partial Fulfillment  
of the Requirements for the Degree  
Master of Science  
Electrical Engineering

---

by  
Xiong Wang  
August 2009

---

Accepted by:  
L. Wilson Pearson, Committee Chair  
Todd Hubing  
Anthony Martin

## ABSTRACT

This thesis discusses spherical near-field measurements implemented by a circular waveguide probe which has much shorter length and wider operating range than those proposed similar circular probes. A brief introduction of spherical near-field measurement techniques is provided first. We also introduce the well-known conclusion that utilizing first-order probes simplifies the measurements and associated near-field to far-field transformation. Accordingly, a relatively short circular waveguide probe antenna is designed and fabricated. Detailed fields of this probe are analyzed to demonstrate that it is still a first-order probe even though the length is short. Furthermore, it radiates only first-order fields over a wide frequency range, indicating it is applicable as a near-field measurement probe in this range. This wide operating range is because of the use of symmetry to control unwanted modes. We also exploit the concept that a first-order probe can be realized with two first-order modes:  $TE_{11}$  and  $TM_{11}$ . Probe calibration results also evidence these findings. This circular waveguide probe is then utilized to examine a base station antenna in its near-field range. The transformed far-field patterns validate the practicability of our probe.

## DEDICATION

I dedicate this thesis to my parents, who love me so much and support my study here. Another source of love is my fiancée, Huijuan, whose encouragement was my hope when my work did not go smoothly.

## ACKNOWLEDGMENTS

I would like to express my gratitude to my advisor Dr. L. Wilson Pearson for his invaluable help during my three years study at Clemson University. It is him who guided me into the area of electromagnetics, a fantastic field that I will devote my life to. My work has gained very substantially from his profound knowledge. It is my pleasure to be a student of him, to learn so much from him, and to be trained to pursue excellence by him.

I also want to thank my committee members Dr. Todd Hubing and Dr. Anthony Martin. They took their precious time to read my thesis and gave helpful suggestions.

## TABLE OF CONTENTS

	Page
TITLE PAGE .....	i
ABSTRACT .....	ii
DEDICATION .....	iii
ACKNOWLEDGMENTS .....	iv
LIST OF TABLES .....	vi
LIST OF FIGURES .....	vii
CHAPTER	
I.    INTRODUCTION TO SPHERICAL NEAR-FIELD MEASUREMENT ....	1
Background of Near-Field Measurement.....	1
Measurement Geometry.....	2
Transmission Formula .....	3
Solving the Transmission Formula .....	5
II.   CIRCULAR WAVEGUIDE PROBE .....	7
Configuration .....	7
Operating Principles.....	10
Fields.....	13
Probe Operating Range .....	22
Calibration of the Probe .....	25
III.  MEASUREMENTS OF A BASE STATION ANTENNA .....	33
Brief Introduction to Antenna.....	33
Measurement Geometry.....	33
Far-Field Patterns from Near-Field Data .....	35
IV.  CONCLUSIONS.....	38
REFERENCES .....	39

## LIST OF TABLES

Table		Page
2.1	Control mechanisms for circular waveguide modes.....	11
2.2	Mode coefficient magnitudes of some modes at several planes for $ka=1.9, 3, 3.83$ and $4.1$ .....	20

## LIST OF FIGURES

Figure	Page
1.1 Probe and AUT minimum spheres and coordinate systems .....	2
2.1 Photo of the probe.....	8
2.2 Longitudinal view of probe structure and components.....	9
2.3 Photo of the dielectric sheet with metal patches .....	9
2.4 Feeding scheme and metal patch dimension.....	10
2.5 Electric field distribution of TE <sub>11</sub> mode.....	11
2.6 Functions of impedance matching .....	13
2.7 Approximate current directions on patches .....	16
2.8 Electric field configurations of some modes having good coupling with currents.....	17
2.9 Electric field configurations of some modes having poor coupling with currents.....	18
2.10 Cutoff values of $ka$ and cutoff frequencies of some modes in the 6-inch probe .....	23
2.11 Power ratio of the third-order to the first-order for different frequencies and different values of $z_a$ .....	25
2.12 Anechoic chamber .....	26
2.13 9.1-inch diameter circular waveguide.....	27
2.14 6-inch AUT on positioner .....	27
2.15 Measurement set-up for 6-in probe calibration.....	28
2.16 6-inch probe far-field principle power patterns at 1.19 GHz.....	29
2.17 6-inch probe far-field principle power patterns at 1.88 GHz.....	29

List of Figures (Continued)

Figure	Page
2.18 6-inch probe far-field principle power patterns at 2.4 GHz.....	30
2.19 6-inch probe far-field principle power patterns at 2.57 GHz.....	30
2.20 Normalized $\mu$ mode power spectrums of the 6-inch probe.....	32
3.1 Photo of the base station antenna.....	33
3.2 Base station antenna mounted on the positioner.....	34
3.3 Base station antenna near-field principle power patterns at 1.8 GHz .....	35
3.4 Base station antenna near-field principle power patterns at 1.9 GHz .....	35
3.5 Base station antenna far-field E-plane power patterns at 1.8 GHz.....	36
3.6 Base station antenna far-field H-plane power patterns at 1.8 GHz.....	36
3.7 Base station antenna far-field E-plane power patterns at 1.9 GHz.....	37
3.8 Base station antenna far-field H-plane power patterns at 1.9 GHz.....	37

## CHAPTER ONE

### INTRODUCTION TO SPHERICAL NEAR-FIELD MEASUREMENT

#### Background of Near-Field Measurement

Antenna testing and characterization has been studied intensively. Antenna measurements can be performed in outdoor range and indoor range. It is relatively easier to accommodate the far-field (Rayleigh) distance of  $2D^2/\lambda$  in an outdoor range. Here,  $D$  is the largest dimension of the test antenna and  $\lambda$  is the wavelength. An indoor range generally employing an anechoic chamber is attractive in many respects, such as suppression of environmental reflection, immunity to adverse weather and resistance to outside interference. However, in a chamber, the separation between the probe and the antenna under test (AUT) may be smaller than the Rayleigh distance. Accordingly, near-field measurement, along with appropriate mathematical operations providing a possibility for deriving the radiation properties of the far-field from the measured information of the near-field, emerged as the solution to this problem.

In accordance with the scanning surfaces of the test antennas, near-field measurements are classified into planar scanning, cylindrical scanning and spherical scanning. Among these groups, spherical scanning is the most popular one and is applied in this work. Spherical near-field testing is developed relatively thoroughly by Hansen [1]. In addition, Jensen, Engen also made considerable contribution to this field. Besides [1], Wittmann and Stubenrauch developed the method in parallel with Hansen and authored a report [2].

The notations in this work and the theoretical derivations in this section follow those in Hansen's book [1], and the same time dependence  $e^{-i\omega t}$  is assumed.

### Measurement Geometry

The near-field measurement geometry is the same as that for far-field measurement except that the measurement distance,  $A$  in Fig. 1.1, is less than the Rayleigh distance. As shown in Fig. 1.1, the coordinate system for the AUT is  $(x,y,z)$  and for probe is  $(x',y',z')$ . A spherical coordinate system is superimposed over the AUT coordinate system and is denoted  $(r,\theta,\varphi)$ . The origin of the probe coordinate system is located in this system as  $(A,\theta,\varphi)$ . Angle  $\chi$ , frequently used in spherical near-field measurements and often called probe orientation angle, is described as the angle resulting from probe's rotation around its  $z'$  axis.

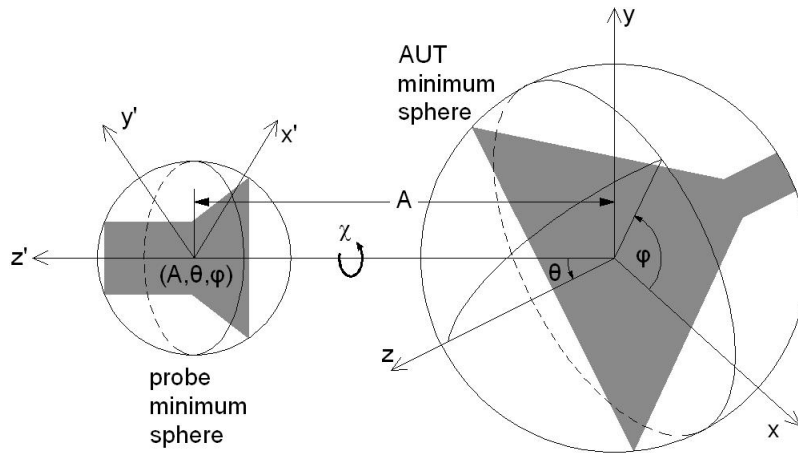


Fig. 1.1. Probe and AUT minimum spheres and coordinate systems. The origin of the primed (probe) coordinates lies at a radius  $A$  in the unprimed (AUT) coordinates and moves around the AUT through variation of  $(\theta, \varphi)$ .

## Transmission Formula

In a spherical near-field measurement, the AUT is assumed to radiate the signal and the probe to receive it. When a measurement is in process, the probe measures the signal over a sphere enclosing the AUT, see Fig. 1.1.

Since we deal with conditions in spherical coordinates, we can use spherical wave functions  $F_{smn}^{(c)}(r, \theta, \varphi)$  [1, p. 13] to build fields. Here, the index  $c$  is related to one of the spherical Bessel function, Neumann function, and Hankel function of the first kind and second kind. The index  $s$  corresponds to the two types of spherical wave functions for a source-free region; the indices  $m$  and  $n$  are the order and degree of the associated Legendre function, respectively.

The relationship between the received signal at the probe and the characteristics of AUT and probe is expressed by the *transmission formula* [1, p. 67] appearing as

$$w(A, \chi, \theta, \varphi) = \frac{v}{2} \sum_{s=1}^2 \sum_{n=1}^{\infty} \sum_{m=-n}^n \sum_{\sigma=1}^2 \sum_{\nu=1}^{\infty} \sum_{\mu=-\nu}^{\nu} T_{smn} d_{\mu m}^n(\theta) C_{\sigma\mu\nu}^{sn(3)}(kA) R_{\sigma\mu\nu}^p e^{im\varphi} e^{i\mu\chi}, \quad (1.1)$$

where  $w$  is the signal received by the probe;  $v$  is the excitation signal on the AUT;  $T_{smn}$  and  $R_{\sigma\mu\nu}^p$  are the AUT transmitting coefficients and the probe receiving coefficients, respectively; and  $d_{\mu m}^n(\theta)$  and  $C_{\sigma\mu\nu}^{sn(3)}(kA)$  are the rotation coefficients and translation coefficients, respectively. Note that indices  $\sigma$ ,  $\mu$  and  $\nu$  have the same meaning as  $s$ ,  $m$  and  $n$ , respectively. The only difference is the former are used for the probe, while the latter are used for the AUT. The infinite series in (1.1) will be truncated in practical use.

We can apply this formula in four different ways:

First, if  $T_{smn}$  is known for AUT and  $R_{\sigma\mu\nu}^p$  is known for probe,  $w(A,\chi,\theta,\varphi)$  is computable for all  $(\theta,\varphi)$ . Furthermore, characteristics of the AUT such as pattern and directivity are also obtainable.

Second, if  $R_{\sigma\mu\nu}^p$  is known for a given probe, then we can use the probe to sample  $w$ , radiated by AUT, on a discrete  $(\theta,\varphi)$  grid over a sphere encircling the AUT.

Third, after the measurement in the second application is conducted, the transmission formula can be solved for the set of  $T_{smn}$  for a given AUT based on the known  $R_{\sigma\mu\nu}^p$ . This procedure is central to spherical near-field measurement and is addressed in the next section.

Fourth, the signal  $w'(A',\chi,\theta,\varphi)$  [1, p. 125] received by any other probe and/or measurement radius  $A'$  can be computed with the  $T_{smn}$  of the AUT and  $R_{\sigma\mu\nu}^p$  of the old probe or  $R_{\sigma\mu\nu}^{p'}$  of the new probe. Then, from the obtained  $w'$ , the AUT pattern for this new radius can be determined.

Probe calibration allows one to obtain  $R_{\sigma\mu\nu}^p$  before these applications are implemented.

The usual near-field measurements aimed at determining the far-field pattern of the AUT are accomplished by the combination of the second, third and fourth ways, with the  $A'$  of the fourth in the far-field range of AUT.

## Solving the Transmission Formula

In view of the two complex trigonometric factors in (1.1), the transmission formula is solved or inverted by means of the inverse discrete Fourier transform algorithm (IDFT) [1, p. 107]. In addition, the orthogonality of the rotation coefficients is also exploited to enable another IDFT process. At least two sets of  $w(A, \chi, \theta, \varphi)$  should be obtained at two different  $\chi$  to make the transmission formula solvable.

The third way in the last section, using probe's coefficients  $R_{\sigma\mu\nu}^p$ , is termed *measurement with probe correction*. Performing probe correction is the general case when we do near-field measurements. However, in some special cases when probes' dimensions are small, we employ *measurement without probe correction*. In this situation, the probe radiation pattern is similar, at least in the solid angle in which the AUT can be illuminated by the probe, to that of an ideal dipole. Therefore, the  $R_{\sigma\mu\nu}^p$  in the transmission formula is substituted by the well-known receiving coefficients of an ideal dipole. Uncorrected measurements were mainly used historically, when people did not know much about probe correction.

When probe size is significant compared with wavelength, probe correction is necessary. All probe correction techniques are defined according to the *probes' order* which is the  $\mu$  index in the transmission formula. The order of a probe is determined from the dominant  $\mu$  *mode power spectrum* of its radiation far-fields, which are obtained from probe calibration. The detailed procedure of generating this spectrum is given in Section 2.5. Theoretically, *first-order probes*, which have significant power only in their first-

order ( $\mu=\pm 1$ ) [1, p. 107], lead to simple probe correction procedures and associated measurements. Furthermore, in practice, many kinds of antennas can be considered as first-order probes when used in proper bandwidths, such as rectangular waveguide antennas, circular waveguide antennas and conical horn antennas. Therefore, a first-order probe is our first choice in spherical near-field measurements.

## CHAPTER TWO

### CIRCULAR WAVEGUIDE PROBE

#### Configuration

As discussed in Chapter 1, a first-order probe is attractive because both measurement and probe correction procedures associated with it are relatively simple. An *open-ended circular waveguide*, carrying dominant  $TE_{11}$  mode, is the customary embodiment of a first-order probe. This is because when  $TE_{11}$  is the only mode present at the waveguide aperture, its radiated field will have power only in the first-order, which will be manifested in Section 2.3.3. The circular waveguide excitation structure in [3] was shown to have good performance. Like other proposed circular waveguides, waveguide in [3] is also very long, and thus cumbersome. However, we will show in this chapter that one can maintain single-mode performance with a shorter waveguide. Generally speaking, any means of excitation of a waveguide produces higher-order modes. Traditionally, one sets the dimension of the guide fix a cutoff frequency that suppresses unwanted modes at the radiating aperture. In this work, we show that even though several modes can propagate in the guide, the use of symmetry at the point of excitation can suppress the modes and lead to orthomode radiation.

We fabricated the *circular waveguide probe* shown in Fig. 2.1. We have calibrated it and employed it as a probe to examine other antennas in their near-field regions.

This probe is designed to be operated at a frequency as low as 1.16 GHz. The inner diameter of the circular tubing is 6 inches, leading to a dominant ( $TE_{11}$ ) mode

cutoff of 1.15 GHz. The probe was first planned to cover the range from 1.16 GHz to 1.9 GHz. Further investigations show that it can operate well as high as around 2.4 GHz, as discussed in Section 2.4.2.



Fig. 2.1. Photo of the probe.

The 12-inch length of the probe is divided into two segments by a thin, circular 6-inch diameter dielectric sheet, seen in the drawing in Fig. 2.2. The sheet, which contains etched excitation probes for the circular waveguide, is visible in Fig. 2.3. The dimensions of the metal patches are given in Fig. 2.4. The segment between excitation probes and the circular aperture is below cutoff for most, but not all modes other than the  $TE_{11}$  mode and serves to attenuate such modes. The modes that can propagate are suppressed with symmetry in the probe configuration as will be shown in Section 2.3.2. In all, the  $TE_{11}$  mode field is much stronger than other modes in the aperture. The other part shorted by the slider plays a role of *resonant cavity* to perform *impedance matching*, as discussed in Section 2.2.2. Moving the slider changes the length of the resonant cavity and the resonant frequency.

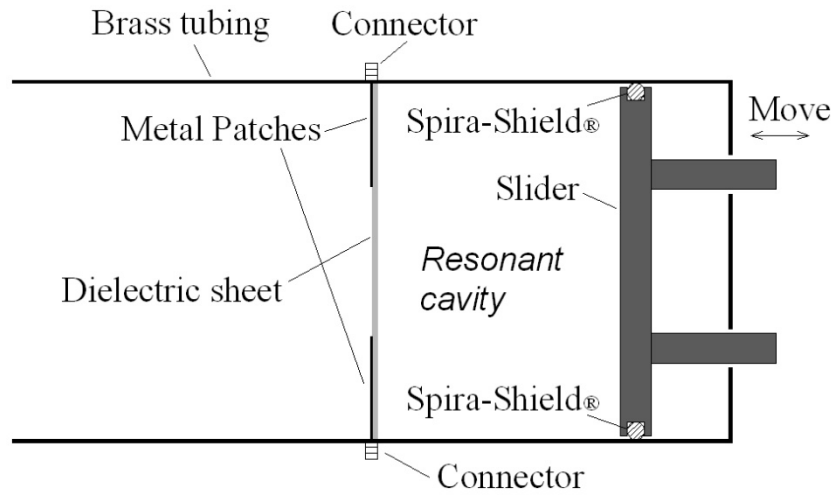


Fig. 2.2. Longitudinal view of probe structure and components.

The dielectric sheet is the ceramic substrate of a circular circuit board. The metal on one side is entirely removed, and on the other side are four metal patches shaped as shown in Fig. 2.4. The center conductor of an SMA connector is soldered to the tapered end of each metal patch, connecting each patch to external devices, like a signal generator or a receiver.

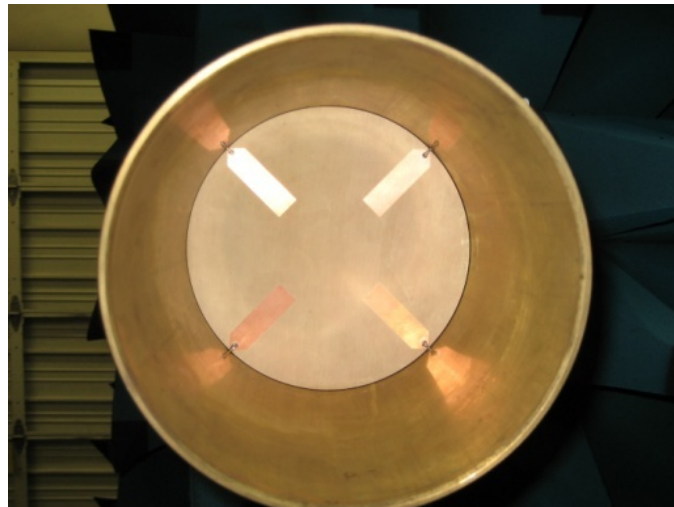


Fig. 2.3. Photo of the dielectric sheet with metal patches.

## Operating Principles

### Excitation

The four feed ports of the waveguide are fed through two  $180^\circ$  hybrid couplers from the four ports. As shown in Fig. 2.4, diametrically opposite ports A and C are connected to the differential mode outputs of a  $180^\circ$  coupler so as to produce vertical polarization, and ports B and D are connected to that of another coupler, producing horizontal polarization. This creates a dual linear polarization antenna.

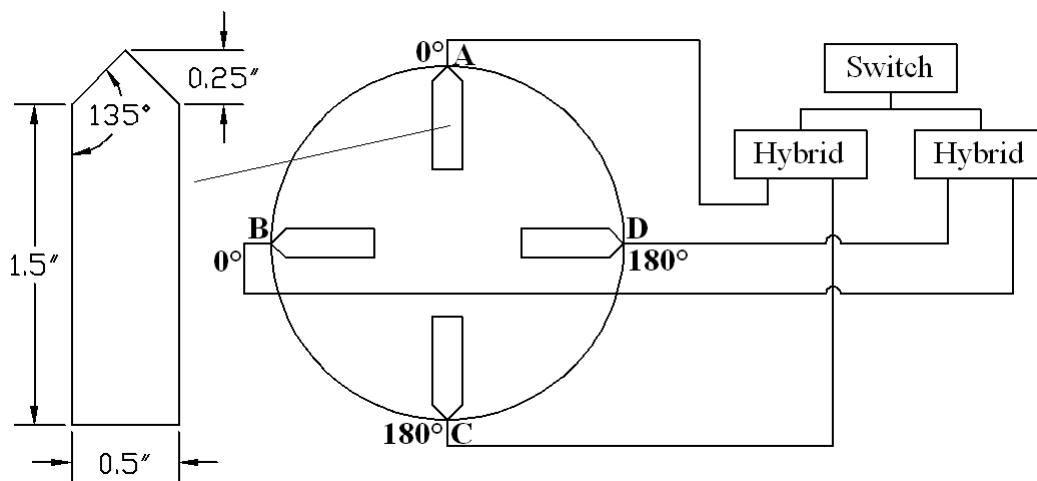


Fig. 2.4. Feeding scheme and metal patch dimension.

The currents flowing on the metal patches stimulate the full spectrum of circular waveguide modes, propagating to both the right and left in Fig. 2.3. Because of the opposite phases and equal magnitudes of the currents on the two diametrically opposite patches, the  $TE_{11}$  distribution, shown in Fig. 2.5, and perhaps a few other modes, will be stimulated most strongly. Some higher-order modes are also stimulated, but are below the waveguide cutoff and are attenuated heavily before they reach the aperture at the left end

of Fig. 2.2. Thus, the aperture is an antenna with a field distribution comprising, at most, a few low-order modes.

Mode	Cutoff Frequency (GHz)	Control Mechanism
TE <sub>11</sub>	1.154	None
TM <sub>01</sub>	1.507	Symmetry
TE <sub>21</sub>	1.914	Symmetry
TE <sub>01</sub>	2.401	Symmetry
TM <sub>11</sub>	2.401	None
TE <sub>31</sub>	2.632	Cutoff
TM <sub>21</sub>	3.218	Cutoff
TE <sub>41</sub>	3.332	Cutoff

Table 2.1. Control mechanisms for circular waveguide modes. The TM<sub>11</sub> mode is not harmful because it is first-order in  $\varphi$ , as will be discussed below.

Table 2.1 shows some modes of a 6-inch diameter circular waveguide in the order of their cutoff frequencies.

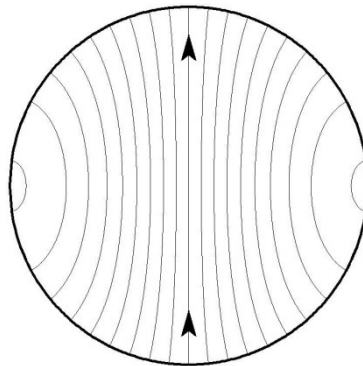


Fig. 2.5. Electric field distribution of TE<sub>11</sub> mode.

It is evident that if this waveguide is operated at a frequency as high as about 2.4 GHz, three unwanted modes  $TM_{01}$ ,  $TE_{21}$  and  $TE_{01}$  must be controlled through the symmetry of the feed rather than by cutoff. The presence of the  $TM_{11}$  in the radiating aperture does not compromise the operation of the probe with only first-order fields. The following discussion explains how the proper symmetry of excitation avoids radiation from unwanted modes.

As seen in Fig. 2.4, two hybrids are configured to excite two pairs of patches  $90^\circ$  apart around the waveguide. By switching the excitation to the two hybrids, one can select between two linear polarizations without rotating the waveguide, and two sets of measurement of orthogonal polarizations can be accomplished with only one set of rotations of the AUT. In our experiments, one hybrid is fed by an input signal while the other is removed, with the two vacant connectors terminated by  $50 \Omega$  loads. Thus, only one field polarization is observed. The two diametrically opposite patches directly connected to the feeding hybrid are termed *the feeding patches*.

### Impedance Matching

The basic function of impedance matching is to minimize the reactance of the total antenna impedance, and accordingly maximize the power radiated from the aperture. As depicted in Fig. 2.6, the total antenna impedance  $Z_t$  is expressed as

$$Z_t = Z_a - jX_c = R_a + j(X_a - X_c), \quad (2.1)$$

where  $Z_a$  is the impedance, containing resistance  $R_a$  and reactance  $X_a$ , looking toward the aperture and  $-X_c$  is the reactance of the cavity. In practice, we will tune the slider to make

the reactive part in (2.1) vanish. On the most ordinary occasions when only one waveguide mode exists, in view of the reflection coefficient of metal is -1, the length  $d$  in Fig. 2.6 should be  $\lambda_g/4$  to occasion resonance. Here  $\lambda_g$  is the guided wavelength for the resonant frequency. In practice, when several modes are often present, the functioning of impedance matching is much more complicated.

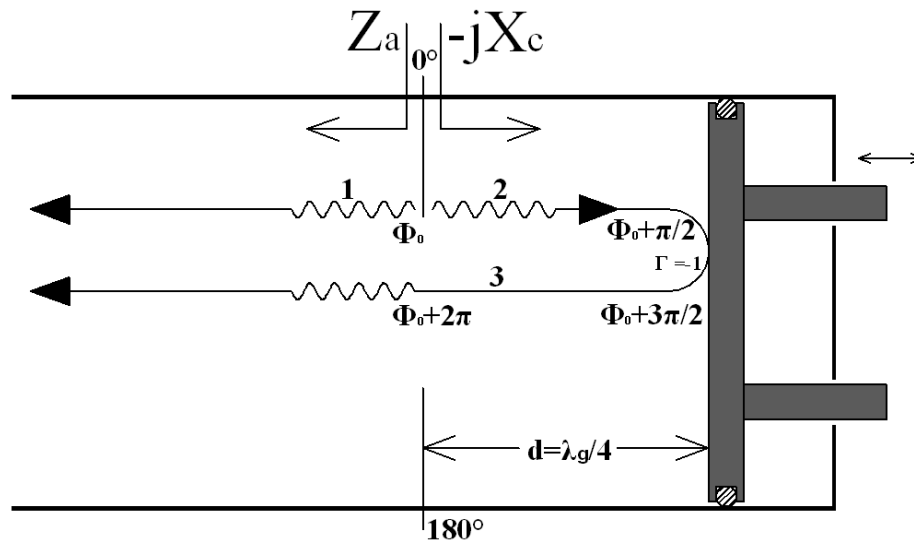


Fig. 2.6. Functions of impedance matching.

## Fields

### Expansion Coefficients

This section deals with deducing the fields in the waveguide created by the input currents. We use the method discussed in Collin [4] to deal with this problem. The method is based on a conclusion that due to the orthogonality of each waveguide mode, the fields stimulated by a current source in a waveguide can be expressed as an infinite series of all the normal modes ( $TE_{mn}$  and  $TM_{mn}$ )

$$\mathbf{E}(x, y, z) = \sum_{m,n}^{\infty} \left[ a_{mn}^{\pm} \mathbf{E}_{mn}^{\pm}(x, y) e^{m\Gamma_{mn}z} + a'_{mn}{}^{\pm} \mathbf{E}'_{mn}{}^{\pm}(x, y) e^{m\Gamma'_{mn}z} \right], \quad (2.2)$$

where  $\mathbf{E}(x, y, z)$  is the total electric field in waveguide,  $\mathbf{E}_{mn}^{\pm}(x, y)$  is the total modal electric field for the  $mn^{\text{th}}$  normalized transverse electric (TE) mode for positive- and negative-going waves and  $\mathbf{E}'_{mn}{}^{\pm}(x, y)$  is the total modal electric field for the  $mn^{\text{th}}$  normalized transverse magnetic (TM) mode for positive- and negative-going waves<sup>1</sup>. These field elements each have corresponding expansion coefficients  $a_{mn}^{\pm}$  and  $a'_{mn}{}^{\pm}$ . The reciprocity principle may be used to solve the expansion coefficients.

For purposes in the present work, the expressions of the expansion coefficients,  $a_{mn}^{\pm}$  and  $a'_{mn}{}^{\pm}$ , for positive- and negative-going modes are written as

$$2a_{mn}^{\pm} = -\iint_S \mathbf{J}(x, y) \cdot \mathbf{E}_{mn}^{\pm}(x, y) dS \quad (2.3a)$$

for TE modes, and

$$2a'_{mn}{}^{\pm} = -\iint_S \mathbf{J}(x, y) \cdot \mathbf{E}'_{mn}{}^{\pm}(x, y) dS \quad (2.3b)$$

for TM modes.

Here,  $\mathbf{J}(x, y)$  (A/m) is the surface current density on an opposing pair of metal patches. We employ the field's properties tabulated in [5] after they are normalized to compute expansion coefficients. The currents are completely transversely distributed, and the plane where the metal patches reside is assigned to be the  $z=0$  plane. From [5],  $a_{mn}^{\pm} = a'_{mn}{}^{\pm}$  can be readily deduced.

---

<sup>1</sup> We have expanded the notation of [4] in an obvious fashion so as to denote explicitly TE and TM modes as well as the wave numbers  $\Gamma$  by unprimed and primed notations respectively.

Exact current density  $\mathbf{J}(x,y)$  on patches can be computed numerically with integral equation techniques. It is adequate for present purposes to develop approximate expressions for  $\mathbf{J}(x,y)$ . First, the current density is taken to having sinusoidal distribution along  $y$  axis in Fig. 2.7, and vanishes at the ends of the patches ( $y=\pm r_0$ ). Second, in view of the patch shape, the current directions are assumed to follow the arrowed lines in Fig. 2.7. Last, the current density magnitude would have no variation upon  $x$  axis and be inversely proportional to the metal width when flow through the quasi-triangular region. Therefore, the current density  $J_1$  and  $J_2$  on the upper and lower patches, respectively, in Fig. 2.7 are specified to be

$$\mathbf{J}_1 = \begin{cases} C \sin[k_0(y-r_0)](-\hat{x} \sin \alpha + \hat{y} \cos \alpha), & r_1 < y < r_2 \\ C \sin[k_0(y-r_0)]\hat{y}, & r_0 < y < r_1 \end{cases} \quad (2.4a)$$

and

$$\mathbf{J}_2 = \begin{cases} -C \sin[k_0(y+r_0)]\hat{y}, & -r_1 < y < -r_0 \\ -C \sin[k_0(y+r_0)](\hat{x} \sin \beta + \hat{y} \cos \beta), & -r_2 < y < -r_1 \end{cases}, \quad (2.4b)$$

where,

$$\alpha = \arctan\left(\frac{x}{a-y}\right), \quad \beta = \arctan\left(\frac{x}{a+y}\right). \quad (2.4c)$$

In (2.4),  $C$  is a constant specified by the amplitude of the input signal,  $k_0$  is the wave number in free space and  $r_0$ ,  $r_1$  and  $r_2$  are indicated in Fig. 2.7.

In practice, (2.2) is truncated to limit the number of terms in the expansion. We will first investigate the relationships between the source currents and the properties of

the modes in waveguide, and then take advantage of the evanescent properties of higher-order modes to choose the number of terms retained in (2.2).

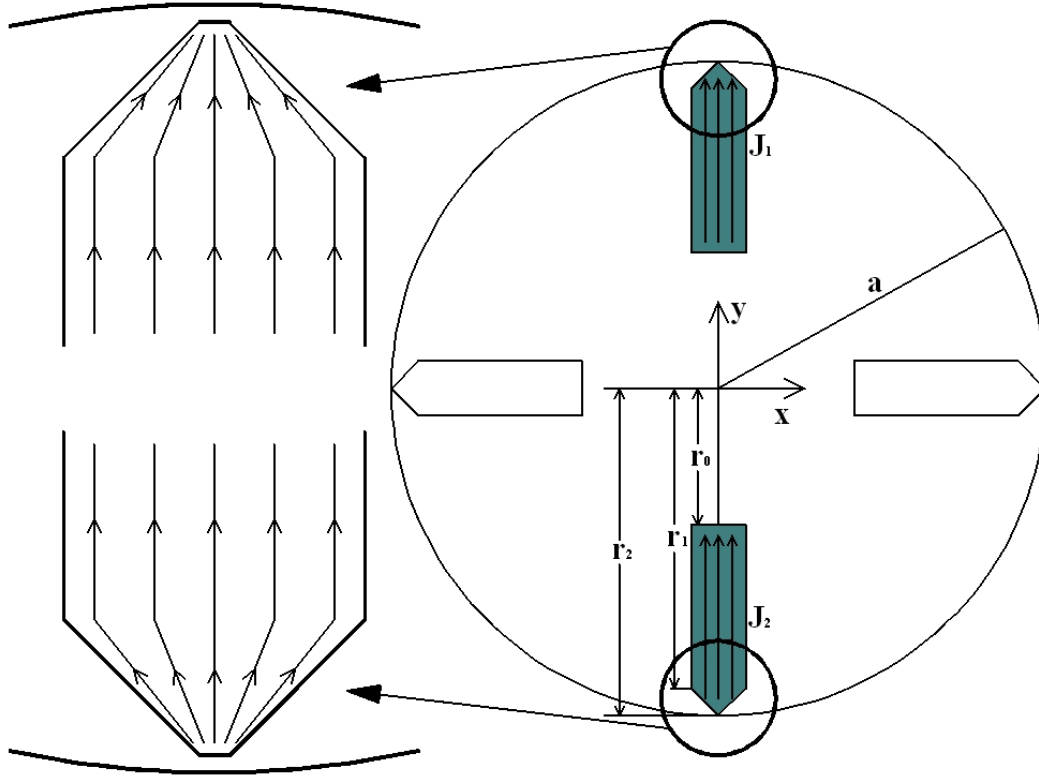


Fig. 2.7. Approximate current directions on patches.

### Fields in the Waveguide

Even though an infinite set of waveguide modes are present to make the series expressions (2.2) complete, symmetry dictates that just part of them can be generated by the source currents in Fig. 2.7 and are meaningful in calculation. This is evident from the dot products in the integrands in (2.3). Based on the notation of [4], the first index of a mode is associated with the circumferential variation of its fields. This is characterized by the  $\varphi$  dependence factor  $\sin(\mu\varphi)$  or  $\cos(\mu\varphi)$  in a mode's field expressions. Here, the index

$\mu$  is the same as the index  $m$  in (2.2). But when we describe something related to  $\varphi$  dependence, we choose  $\mu$  to make it consistent with the similar concepts in probe radiation fields. In Figs. 2.8 and 2.9, we can assume that  $\varphi=0$  is defined by a line horizontal and pointing to the right. Thus,  $E_\rho$  has  $\sin(\mu\varphi)$  dependence in all three parts of Fig. 2.8. In the (a) and (b) parts of Fig. 2.9,  $E_\rho$  exhibits  $\cos(\mu\varphi)$  variation. The TE<sub>12</sub> mode in Fig. 2.9 (c) has no  $E_\rho$  component at all. We observe that modes with odd first indexes  $\mu$  are more strongly coupled with the patch currents shown in Fig. 2.7. We term these modes *odd modes* in waveguide. The modes with  $\mu=1$  are termed the *first-order modes*, modes with  $\mu=3$  are termed the *third-order modes*, and so on. Besides TE<sub>11</sub>, the electric field configurations of some other odd modes whose electric field lines' directions are coincident with the patch currents' directions in Fig. 2.7 are listed in Fig. 2.8.

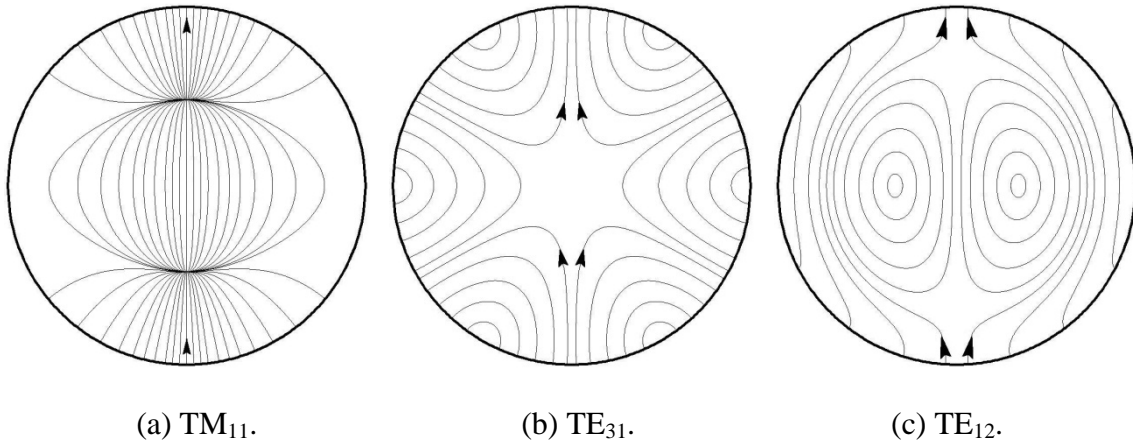


Fig. 2.8. Electric field configurations of some modes having good coupling with currents.

The *even modes*, whose first indexes are even, are excited very weakly by the source currents because their electric field lines' directions are nearly orthogonal to the direction of the current or else antisymmetry exists between the directions on the two

patches. Thus, expansion coefficients of these modes are quite small and we will not consider these modes in practical computation. Electric field configurations of some of the even modes are shown in Fig. 2.9.

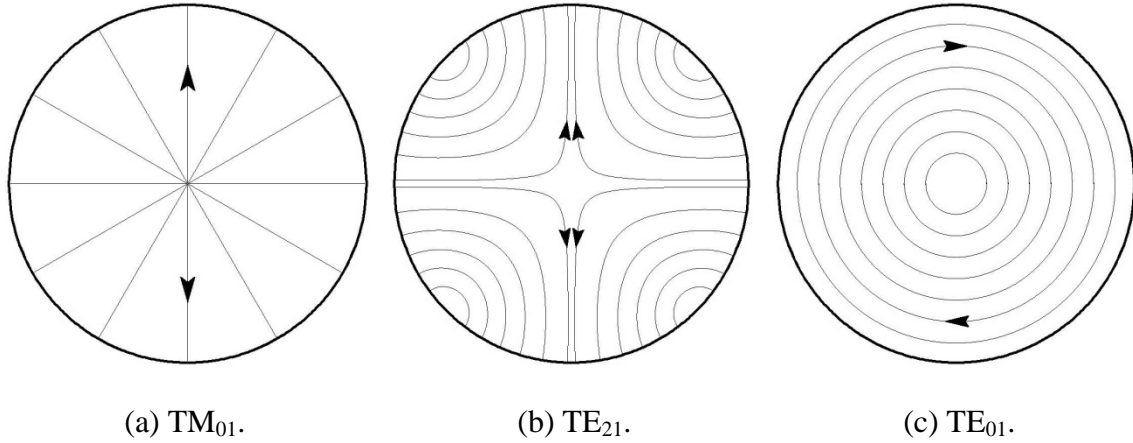


Fig. 2.9. Electric field configurations of some modes having poor coupling with currents.

So far, we have reduced the infinite set of modes in (2.2) to only odd modes, which is still an infinite set. We proceed to consider further the fields made up of odd modes in waveguide. In the expansion (2.2), the  $z$ -dependence of the summands is carried in the  $e^{m\Gamma_{mn}z}$  and  $e^{m\Gamma'_{mn}z}$ . All but a few low-order modes are evanescent, and the distance from the probes to the radiating aperture of the antenna causes quite strong decay in these modes.

Actually, all odd modes can be produced by the source currents. They work together to provide detail in the extremely complicated fields localized around the patches. But most of them are evanescent for a specific operating frequency and will attenuate exponentially along the waveguide. The further their cutoff frequencies are from the operating frequency the faster they will fade away. Therefore, most of the

evanescent modes are negligible at the aperture regardless of their expansion coefficients, and they are computationally meaningless compared with propagating modes. Besides the propagating modes, the first few evanescent modes whose cutoff frequencies are near the operating frequency may not attenuate rapidly enough and need to be considered.

We can identify in (2.2) what we term the *mode coefficient*, as the products  $a_{mn}^{\pm} e^{m\Gamma_{mn} z_a}$  and  $a_{mn}^{\prime\pm} e^{m\Gamma'_{mn} z_a}$ , with  $z_a$  the distance from the plane of the patches to the aperture.

The magnitudes of the mode coefficients of some modes for  $ka = 1.9, 3$  and  $4.1$ , when transmitting from the patches to the aperture, are recorded from  $z=0$  (patches) to  $z=2a$  (aperture) in step of  $z=2a/3$  and tabulated in Table 2.2. All of the coefficients are normalized by the coefficients for  $TE_{11}$ . For the 6-inch diameter probe,  $ka = 1.9, 3, 3.83$  and  $4.1$  corresponds to 1.19 GHz, 1.88 GHz, 2.4 GHz and 2.57 GHz.

Table 2.2 explicitly illustrates that almost all of the evanescent modes except  $TE_{31}$  are excited with significant coefficients at the patches, but they become insignificant due to evanescent propagation. Consequently, we must limit operation of the antenna to frequencies where the  $TE_{31}$  mode is far enough below cutoff to be insignificant. As pointed out in Section 2.1, evanescent propagation from the plane of the patches to the aperture increases the purity of  $TE_{11}$  field.

All of the forgoing may be scaled to new waveguide diameters in a direct fashion so long as the patch size scales with the waveguide diameter.

In conclusion, although the field expression in (2.2) contains infinite modes, even modes do not emerge due to their weak coupling to the source currents. Most of the

$ka$	Modes	TE <sub>11</sub>	TM <sub>01</sub>	TE <sub>21</sub>	TM <sub>11</sub>	TE <sub>01</sub>	TE <sub>31</sub>	TE <sub>12</sub>	TM <sub>31</sub>
(f (GHz))	$p$	1.84	2.4	3.05	3.83	3.83	4.2	5.33	6.38
<b>1.9</b> (1.19)	$z=0$	1	0	0	0.681	0	0.451	0.01	0.506
	$z=2a/3$	1	0	0	0.074	0	0.037	<0.001	0.009
	$z=4a/3$	1	0	0	0.008	0	0.003	<0.001	<0.001
	$z=2a$	1	0	0	0.001	0	<0.001	<0.001	<0.001
<b>3</b> (1.88)	$z=0$	1	0	0	0.793	0	1.126	0.009	0.624
	$z=2a/3$	1	0	0	0.162	0	0.159	<0.001	0.015
	$z=4a/3$	1	0	0	0.033	0	0.022	<0.001	<0.001
	$z=2a$	1	0	0	0.007	0	0.003	<0.001	<0.001
<b>3.83</b> (2.4)	$z=0$	1	0	0	0.156	0	1.717	0.011	0.482
	$z=2a/3$	1	0	0	0.146	0	0.543	0.001	0.016
	$z=4a/3$	1	0	0	0.135	0	0.172	<0.001	0.001
	$z=2a$	1	0	0	0.125	0	0.054	<0.001	<0.001
<b>4.1</b> (2.57)	$z=0$	1	0	0	0.531	0	2.44	0.021	0.432
	$z=2a/3$	1	0	0	0.531	0	1.325	0.002	0.017
	$z=4a/3$	1	0	0	0.531	0	0.719	<0.001	0.001
	$z=2a$	1	0	0	0.531	0	0.39	<0.001	<0.001

Table 2.2. Mode coefficient magnitudes of some modes at several planes for  $ka=1.9, 3, 3.83$  and  $4.1$ .  $p$  are the roots of Bessel function  $J_m(p)=0$  for TM modes and derivatives of Bessel function  $J_m'(p)=0$  for TE modes.  $p$  can also be viewed as *cutoff*  $ka$ , since modes can only propagate when  $ka$  is larger than its  $p$ .

generated odd modes are evanescent and will die out rapidly as the wave travels. Consequently, all of the odd propagating modes and the first one or two odd evanescent modes whose cutoff frequencies are close to the operating frequency are sufficient in computation. This serves as the truncation standard.

### Radiated Fields

Several techniques based on the Weiner-Hopf method have been proposed to deal with radiation from an open-ended circular waveguide. The most accurate development is likely that of Weinstein [6]. It takes into consideration the currents on the outside wall of the circular waveguide and the diffraction at its open end. Another work [7] based on [6] gives results showing good agreement between measured data and theoretical calculations based on Weinstein's solution. We will use the results given in [6] to generate the analytical far-fields of the probe.

From the obtained electric far-fields, we can deduce the power contained in each mode and construct its  $\mu$  mode power spectrum, which indicates the probe's order.

It is also possible to determine the order of the probe without involving the entire complicated calculation of the far-fields using [6]. The trigonometric function  $\varphi$  dependence factors in the field expressions in [6, 7] are taken advantage of to simplify the work. Similar to the function of the factor  $\sin(\mu\varphi)$  or  $\cos(\mu\varphi)$  in a mode's field expressions in a circular waveguide, such factors in the radiated far-field expressions also designate the order of the far-field. Therefore, since the far-field expressions of source

aperture field including only  $TE_{11}$  mode have the factor  $\sin(\varphi)$  or  $\cos(\varphi)$  [6, 7], the far-field is certainly first-order and so is the probe.

### Probe Operating Range

#### Basic Operating Range

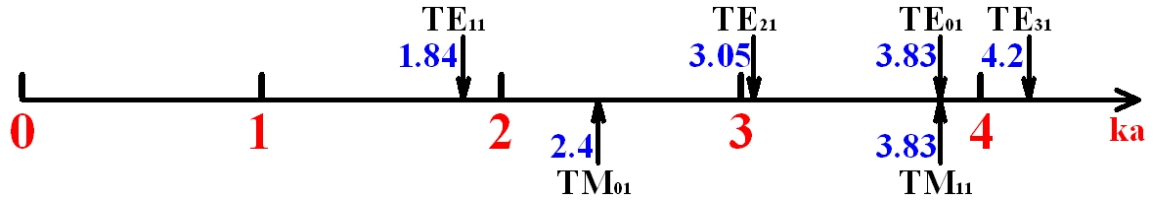
The upper limit of the operating range of a circular waveguide probe is typically chosen to fall below the cutoff frequency of the second propagating mode ( $TM_{01}$ ),  $f_{cTM_{01}}$ . This frequency is 1.51 GHz for the 6-inch probe, making the operating range of the probe about 0.35 GHz. Circular waveguide's major disadvantage is a narrow operating range when operating range is based on this criterion.

#### Extended Operating Range

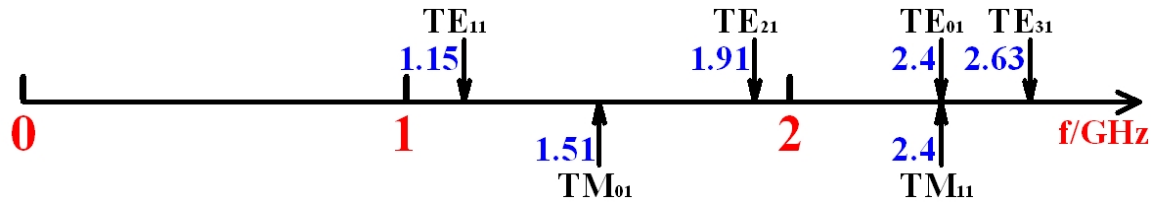
Any probe that manifests the first-order property discussed above is suited for near-field measurements. Consequently, the requirement that only  $TE_{11}$  be admitted into propagation is not necessary. Higher-order modes can be excluded from propagation using the cutoff phenomenon in the traditional way; but they can also be excluded by designing the excitation of the waveguide so as not to launch unwanted modes in the first place as discussed in Section 2.3.2, thereby extending the operating range of our probe.

In Section 2.1, an initial estimate of the probe operating range was described to be 1.16 GHz~1.9 GHz, with 1.9 GHz being just below  $f_{cTE_{21}}$ , when the probe was designed. This is based on the reasoning in Section 2.3.2, which indicates that even though the  $TM_{01}$  mode begins to propagate at 1.507 GHz, it is weakly excited by the probes and does not

appear at the aperture at a significant level. This suggests that the probe could be used without concern of unwanted modes until the  $TE_{21}$  mode begins to propagate at 1.914 GHz.



(a) Cutoff  $ka$ .



(b) Cutoff frequency.

Fig. 2.10. Cutoff values of  $ka$  and cutoff frequencies of some modes in the 6-inch probe.

We can continue to take advantage of the orthogonality between the probe currents and succeeding modes, displayed in Fig. 2.10, to extend the operating frequency upward to further broaden the operating range. As discussed in Section 2.3.2,  $TE_{21}$  and  $TE_{01}$  are not stimulated by the patch currents by a fraction, and therefore are not detrimental to the purity of  $TE_{11}$  fields. As shown in Table 2.2,  $TM_{11}$  has some coefficients whose values are significant compared with those of the  $TE_{11}$  mode when frequency is high and thus affects the  $TE_{11}$  field distribution in the waveguide and at the aperture. However, the  $TM_{11}$  is a first-order mode and does not affect the order of the field at the aperture and a probe radiating both  $TE_{11}$  and  $TM_{11}$  modes is still a first-order

probe. Moreover, the power carried by the  $TM_{11}$  mode contributes to the power of the first-order mode, and helps to increase the total first-order power. Finally, the upper boundary of the practicable bandwidth may approach or go beyond  $f_{cTM_{11}}$ , 2.401 GHz for 6-inches probe. The next mode  $TE_{31}$  is undesired for a first-order probe. We need to find how close to  $f_{cTE_{31}}$  the probe can work. It is evident that the upper frequency of the operating range depends on a specific accuracy requirement, which is how much third-order mode power can be accepted. The third-order mode's power is considered relative to the first-order modes' power comprising  $TE_{11}$  and  $TM_{11}$ . The power ratios of third-order to first-order for different frequencies is expressed as

$$\frac{\text{Third-order power}}{\text{First-order power}} = 10 \log_{10} \left[ \frac{\text{TE}_{31} \text{ power}}{\text{TE}_{11} \text{ power} + \text{TM}_{11} \text{ power}} \right] = 10 \log_{10} \left[ \frac{|a_{31}^+ e^{-\Gamma_{31} z_a}|^2}{|a_{11}^+ e^{-\Gamma_{11} z_a}|^2 + |a_{11}^{\prime+} e^{-\Gamma_{11} z_a}|^2} \right]. \quad (2.5)$$

This expression is based on the normalization of (2.2) and orthogonality among the modes. The three mode coefficients are chosen to be positive-going modes. (2.5) is also applicable to negative-going modes. Power ratio from 2 GHz to 2.6 GHz is plotted in Fig. 2.11. Different required precisions in applications can find their usable upper frequencies in Fig. 2.11. Besides the 6-inch length  $z_a$  from the feeding patches to the aperture, we also investigated the situations for  $z_a$  of 8-inch and 10-inch for applications demanding higher accuracies and wider operating ranges.

Once close to or beyond  $f_{cTE_{31}}$ ,  $TE_{31}$  will not be sufficiently attenuated, and the probe will no longer be a first-order probe. For our work, we have chosen to allow, at

most, -25 dB relative third-order power. Accordingly the usable operating range for us is from 1.16 GHz to 2.4 GHz.

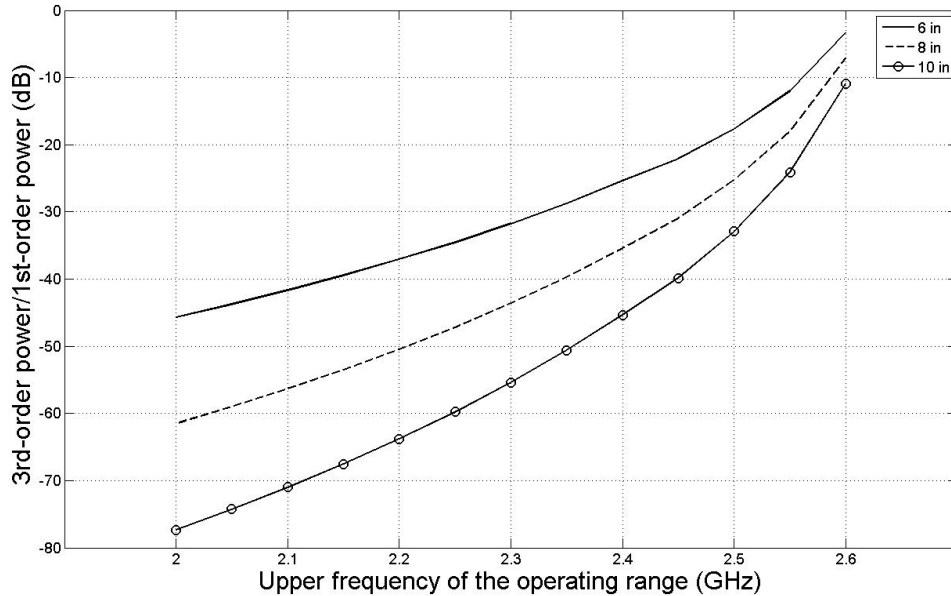


Fig. 2.11. Power ratio of the third-order to the first-order for different frequencies and different values of  $z_a$ .

### Calibration of the Probe

The measurement or calibration of the circular waveguide probe is performed in an anechoic chamber as shown in Fig. 2.12.

Before the probe is measured, the resonant cavity should be adjusted to make the impedance matched. The mixture of several modes, as discussed in Section 2.2.2, complicates the analysis of resonance mechanism because of the diversity of their guided wavelengths, mode coefficients, and phase velocities. Thus, we avoid theoretical derivation of the resonance cavity lengths and simply tune the cavity manually.

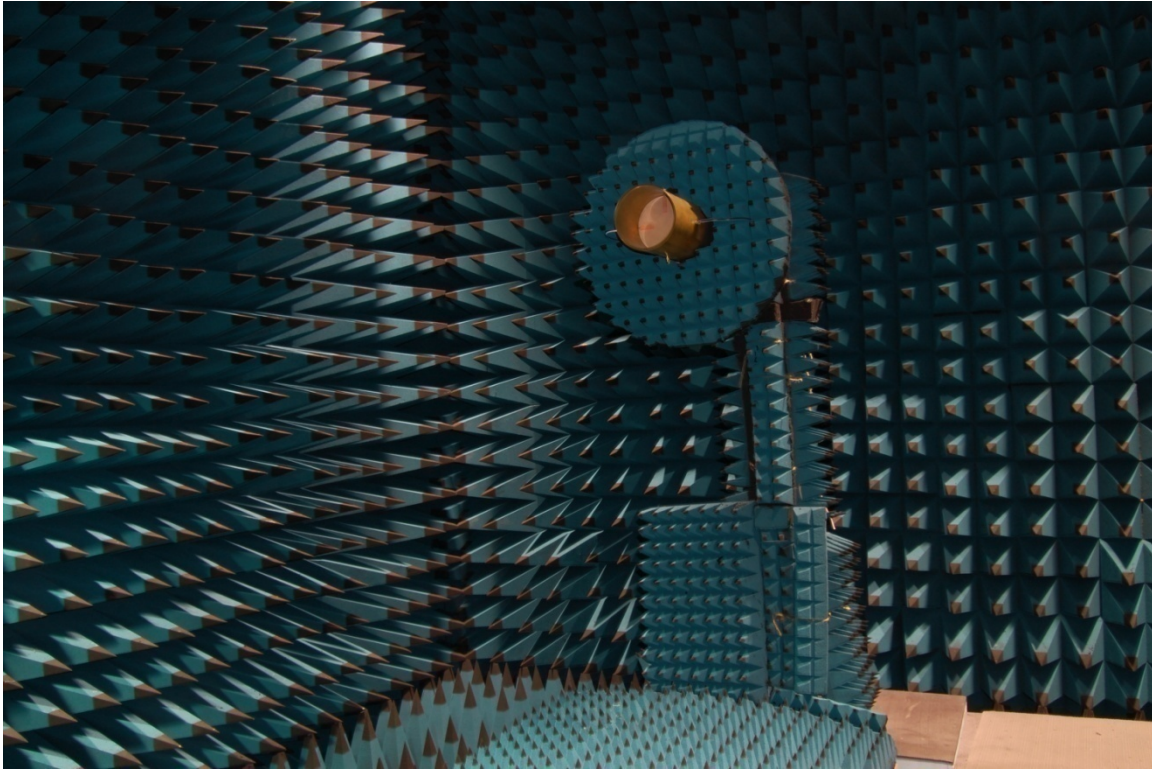


Fig. 2.12. Anechoic chamber.

The 6-inch circular waveguide probe was calibrated by another almost identical circular waveguide antenna with a 9.1-inch diameter, shown in Fig. 2.13. As concluded in Section 2.3.2, the properties of the 6-inch antenna are applicable for this 9.1-inch antenna so long as its length and the properties of the metal patches are scaled properly. Obviously, another hybrid coupler should be introduced to control the excitation of this new waveguide antenna. It can function beyond 760 MHz, and thus covers the entire operating bandwidth of the 6-inch probe. Similar to the 6-inch one, the 9.1-inch probe also has a resonant cavity, which should be tuned to work as well.

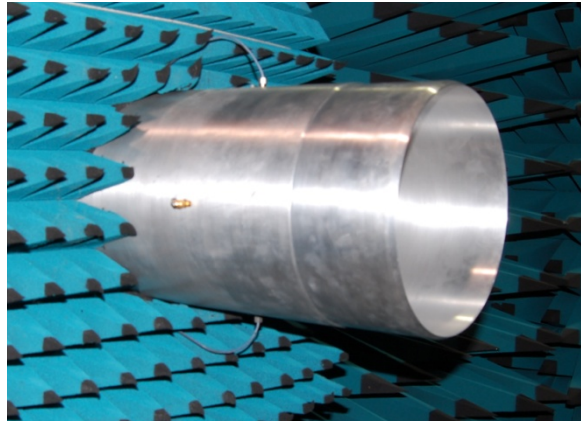


Fig. 2.13. 9.1-inch diameter circular waveguide.

When the 6-inch probe is being measured, it is antenna under test (AUT), while the 9.1-inch antenna plays the role of a probe. In the following part of this section, if not specified, *probe* denotes the 9.1-inch antenna, while *AUT* means the 6-inch antenna.

Measurements are performed with a vertically polarized probe to sample  $E_{\phi}$  and horizontally polarized probe to capture  $E_{\theta}$  of the AUT.

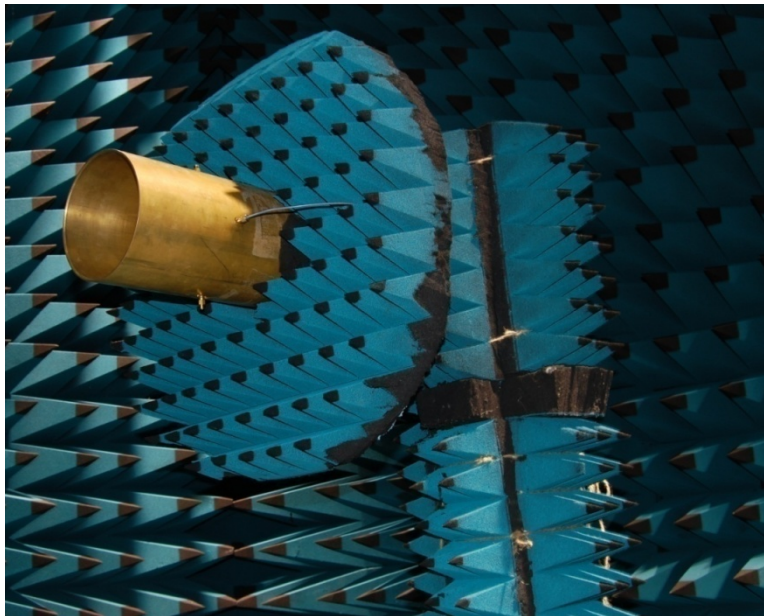


Fig. 2.14. 6-inch AUT on positioner.

During measurements, the probe is immobilized while the AUT is mounted on a positioned as shown in Fig. 2.14 to rotate to generate  $\theta$  and  $\varphi$  variations. The probe's axis is always coincident with the boresight and its aperture is pointing at the AUT. Since the AUT's aperture is the main radiating part, we make the rotation axis of  $\theta$  coplanar with the aperture, shown in the measurement set-up in Fig. 2.15. When  $\theta=0$ , the axis of the AUT is on the boresight. After we finish the measurement with one polarization of the probe, it is rotated  $90^\circ$  to do measurements of the other polarization.

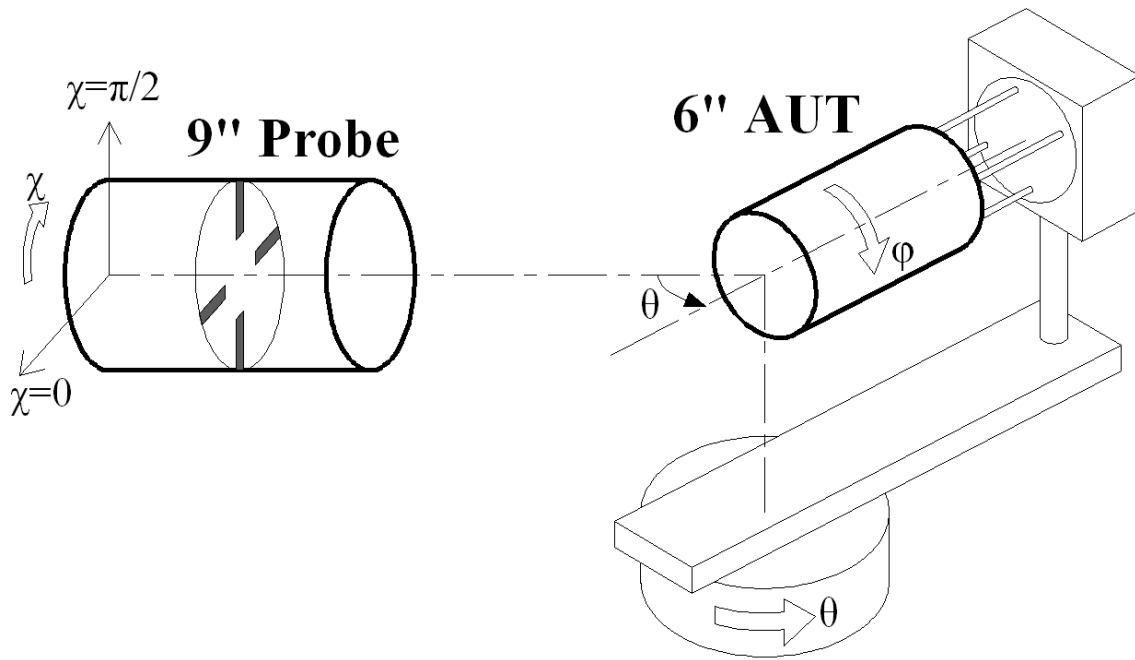


Fig. 2.15. Measurement set-up for 6-in probe calibration.

The separation between the apertures of the probe and the AUT is 1.76m. It is easy to calculate that this distance is far beyond the Rayleigh distance for the AUT working at even 2.6 GHz. Thus, the measurements are conducted in the far-field range of

the AUT. The steps of  $\theta$  and  $\varphi$  are both made to be  $2.5^\circ$ , which was proved to be accurate enough for this far-field measurement.

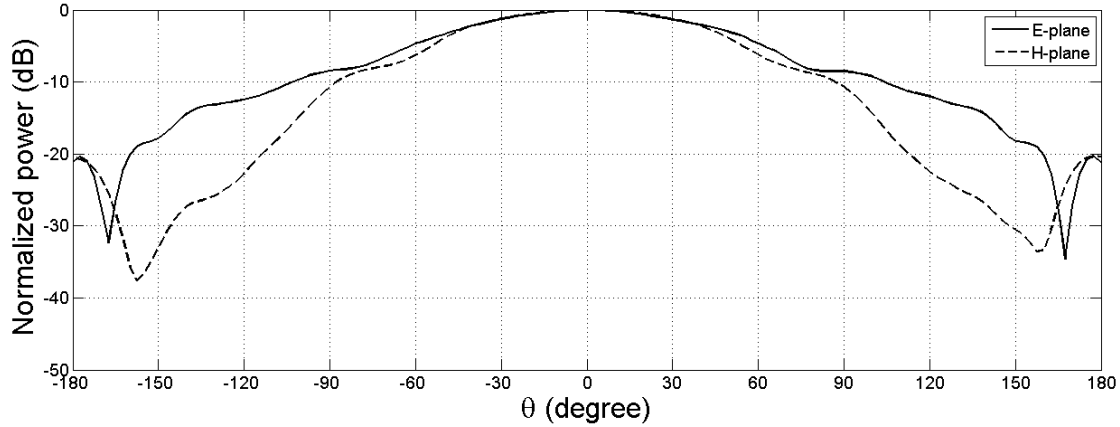


Fig. 2.16. 6-inch probe far-field principle power patterns at 1.19 GHz.

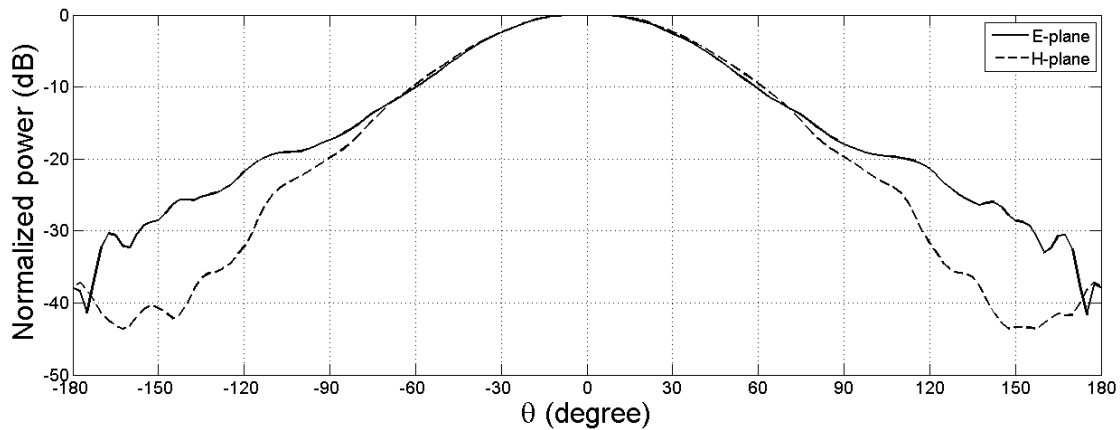


Fig. 2.17. 6-inch probe far-field principle power patterns at 1.88 GHz.

We make the probe transmit power and the AUT receive it, which is opposite to the case in Chapter 1. However, based on reciprocity, they are equivalent.

Measurements were performed at 1.19 GHz, 1.88 GHz, 2.4 GHz and 2.57 GHz, identical to those in Table 2.2. After the measured data are processed, we obtain the far-field power patterns of the AUT shown in Fig. 2.16 to Fig. 2.19.

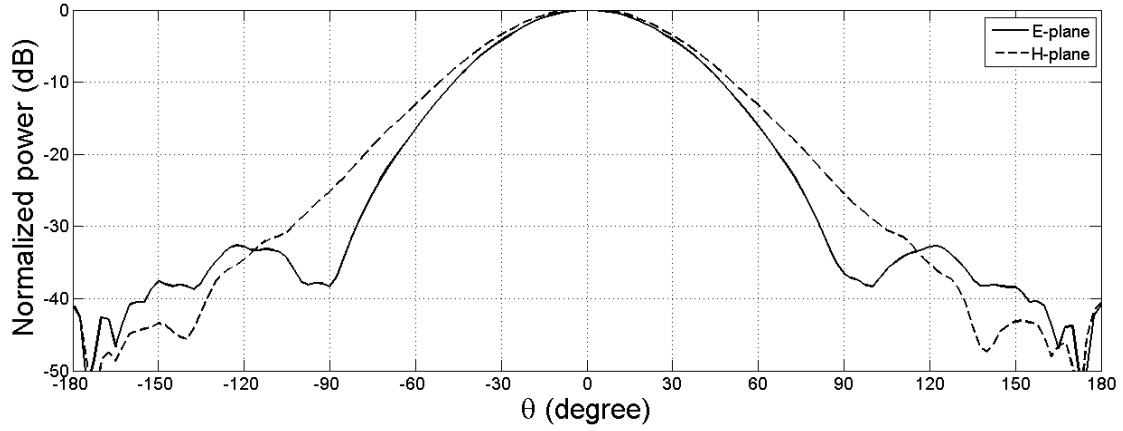


Fig. 2.18. 6-inch probe far-field principle power patterns at 2.4 GHz.

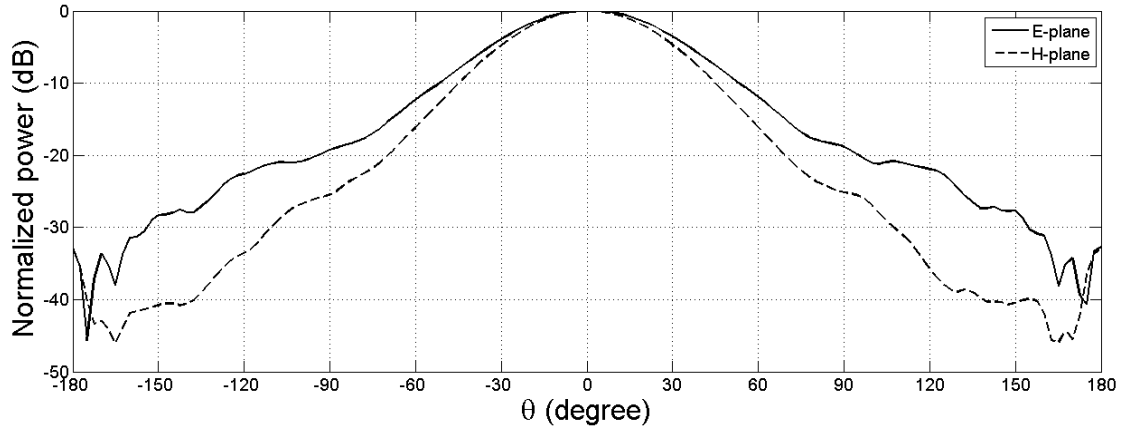


Fig. 2.19. 6-inch probe far-field principle power patterns at 2.57 GHz.

We can also calculate the  $\mu$  mode power spectrum of the radiation fields for each frequency to determine the probe's order. This process is described below.

We start from the calibration data of the 6-inch probe, i.e. its measured electric fields, which have  $\theta$  component and  $\varphi$  component. We express  $E_\theta$  and  $E_\varphi$  in the form of the spherical wave expansion [1, p. 63] as

$$E_\theta(r, \theta, \phi) = k\sqrt{\eta} \sum_{\sigma\mu\nu} Q_{\sigma\mu\nu} \mathbf{F}_{\sigma\mu\nu}^{(3)}(r, \theta, \phi) \cdot \hat{\boldsymbol{\theta}} \quad (2.6)$$

and

$$E_\phi(r, \theta, \phi) = k\sqrt{\eta} \sum_{\sigma\mu\nu} Q_{\sigma\mu\nu} \mathbf{F}_{\sigma\mu\nu}^{(3)}(r, \theta, \phi) \cdot \hat{\boldsymbol{\phi}}, \quad (2.7)$$

where,  $\eta$  is the intrinsic impedance and  $k$  is the propagation constant. The coefficients  $Q_{\sigma\mu\nu}$  are to be solved by the orthogonality [1, p. 330] of the spherical wave functions  $\mathbf{F}_{\sigma\mu\nu}^{(3)}(r, \theta, \phi)$ . The final solution of  $Q_{\sigma\mu\nu}$  is

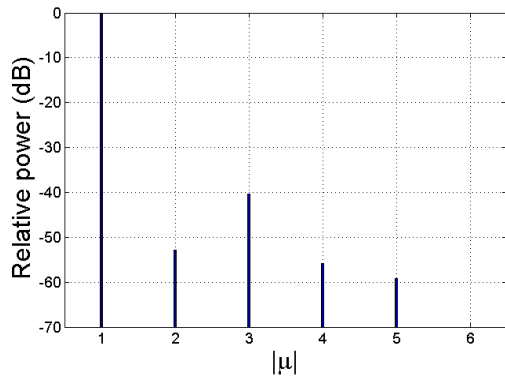
$$Q_{\sigma\mu\nu} = \frac{(-1)^\mu}{k\sqrt{\eta} [R_{\sigma\nu}^{(3)}(kr)]^2} \int_{\phi=0}^{2\pi} \int_{\theta=0}^{\pi} \left[ E_\theta \left( \mathbf{F}_{\sigma,-\mu,\nu}^{(3)}(r, \theta, \phi) \cdot \hat{\boldsymbol{\theta}} \right) + E_\phi \left( \mathbf{F}_{\sigma,-\mu,\nu}^{(3)}(r, \theta, \phi) \cdot \hat{\boldsymbol{\phi}} \right) \right] \sin\theta d\theta d\phi \quad (2.8)$$

The function  $R_{\sigma\nu}^{(3)}(kr)$  in (2.8) is defined in [1, p. 314]. This expression may be evaluated from measured field data using numerical integration. The power contained by all modes with the same  $|\mu|$  in the radiation fields is expressed by [1, p. 236]

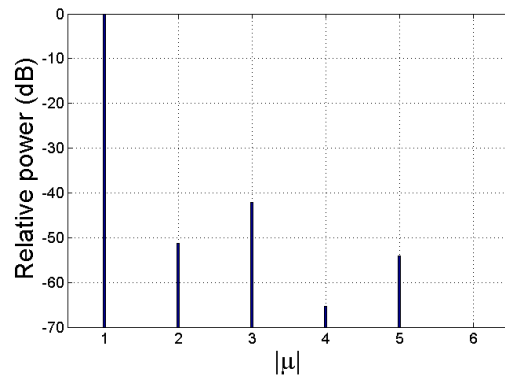
$$P_{rad}^{(\mu)} = \frac{1}{2} \sum_{\sigma=1,2} \sum_{\mu'=-\mu,\mu} \sum_{\nu=\mu}^{\nu_{\max}} |Q_{\sigma\mu'\nu}|^2, \quad \mu \geq 0. \quad (2.9)$$

The  $\mu$  mode power spectrums, normalized by the power of the first-order modes, are given in Fig. 2.20.

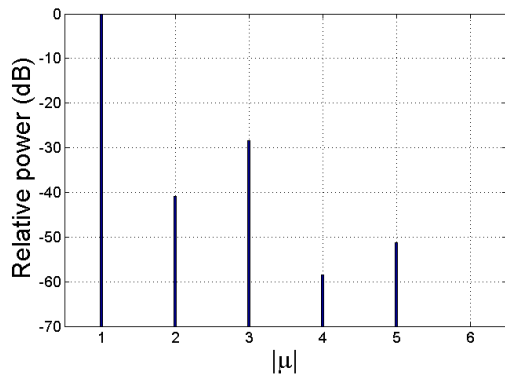
One sees from Fig. 2.20, the 6-inch probe is a first-order probe in the range from 1.19 GHz to 2.4 GHz, since the third-order mode power is negligible based on our accuracy requirement. At 2.57 GHz, the TE<sub>31</sub> mode radiates significant power relative to the first-order modes and the 6-inch probe is no longer a first-order probe. These results verify the reasoning in Sections 2.3.2 and 2.4.2.



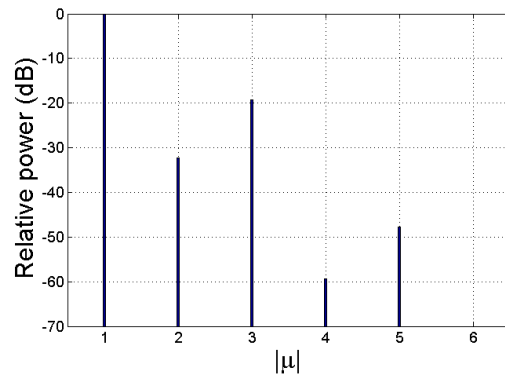
(a) 1.19 GHz.



(b) 1.88 GHz.



(c) 2.4 GHz.



(d) 2.57 GHz.

Fig. 2.20. Normalized  $\mu$  mode power spectrums of the 6-inch probe.

CHAPTER THREE  
MEASUREMENTS OF A BASE STATION ANTENNA

Brief Introduction to Antenna

A base station antenna used for wireless communication, shown in Fig. 3.1, will be measured by our 6-inch circular waveguide first-order probe. Its length is 1.86 m and can operate from 1.8 GHz to 2.1 GHz.



Fig. 3.1. Photo of the base station antenna.

Measurement Geometry

We use a specialized positioner, shown in Fig. 3.2, to facilitate the mounting of this long antenna. It is noteworthy that the masts of this antenna and the drive mechanism through the mast are altogether dielectric. It is obvious that the coordinate system is different from the one used when calibrating the circular waveguide probe in Chapter 2. Change in the coordinate system does not affect any theory in Chapter 1, because the long antenna is also measured on a sphere fully enclosing it. Note that it is tilted by an angle  $4^\circ$  when being mounted on the aluminum pipe in Fig. 3.2. This emulates the conditions when it is hung on a tower with declination.

Measurements are performed at 1.8 GHz and 1.9 GHz. Thus, the antenna is measured in its near-field region. Since we are using a first-order probe, only two sets of measurement are needed, with the probe vertically and horizontally polarized respectively. The angular increase of  $\theta$  and  $\varphi$  are both set to  $3^\circ$ , which is adequately accurate for the antenna size and frequency.

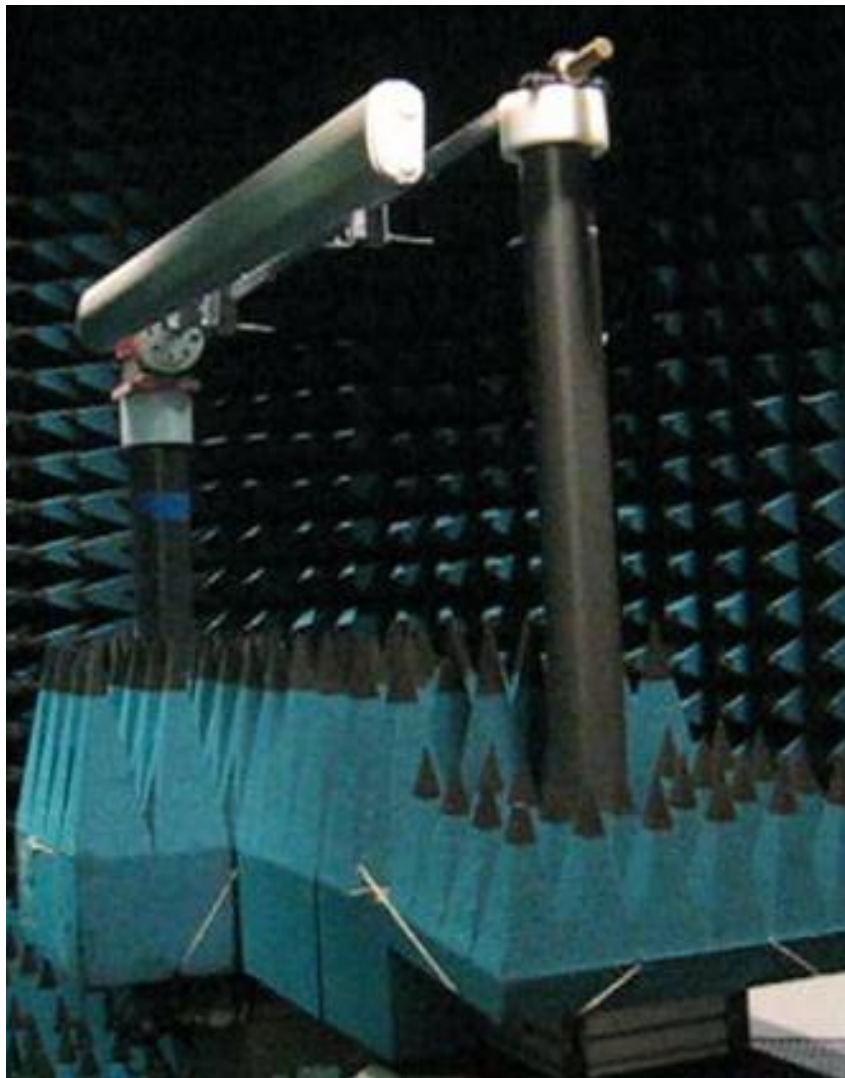


Fig. 3.2. Base station antenna mounted on the positioner.

## Far-Field Patterns from Near-Field Data

The measured near-field patterns are given in Fig. 3.3 and Fig. 3.4.

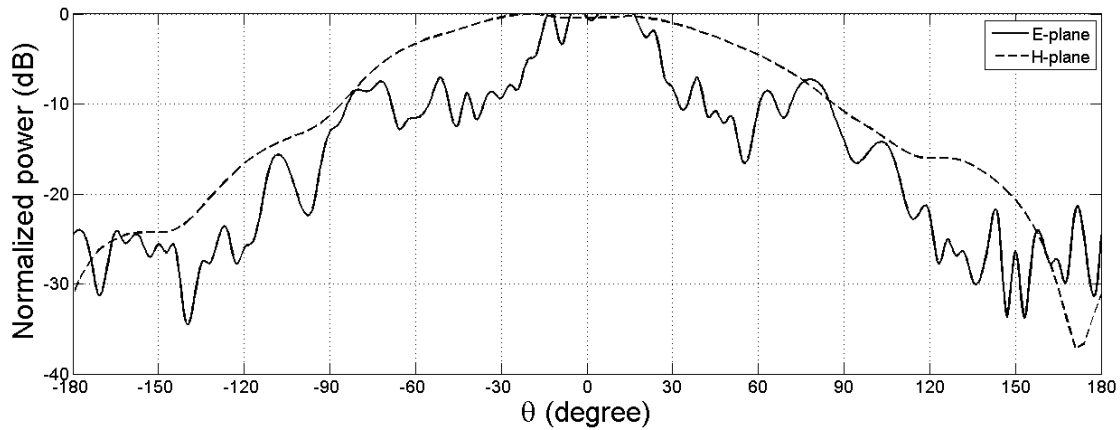


Fig. 3.3. Base station antenna near-field principle power patterns at 1.8 GHz.

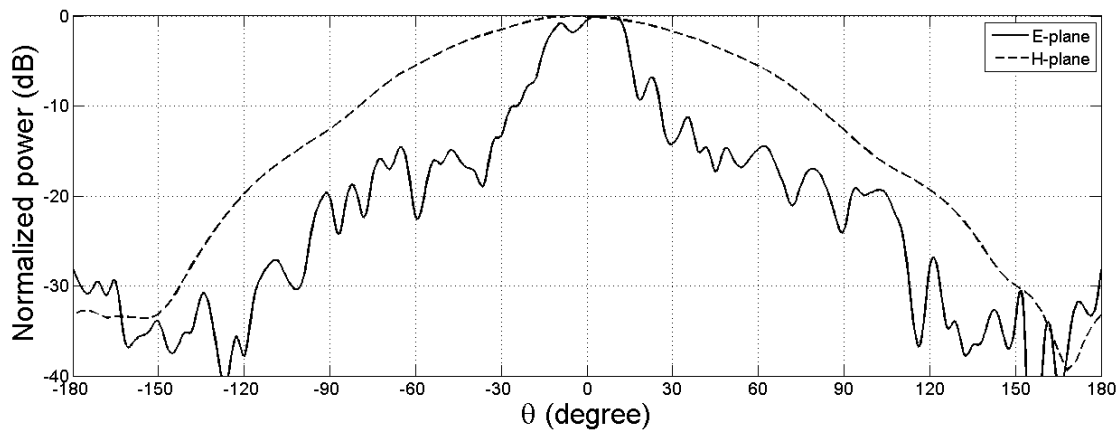


Fig. 3.4. Base station antenna near-field principle power patterns at 1.9 GHz.

We can then implement a near-field to far-field transformation to generate the far-field pattern of the base station antenna. It is evident that the calibration data of the 6-inch probe at 1.8 GHz and 1.9 GHz should be already available now. During the transformation process, the properties of the 6-inch probe is utilized to accomplish probe

correction. This is operated by the software TICRA imbed in MI 3000. The corresponding transformed far-field patterns and published measured far-field patterns of the same type of antenna are plotted in Figs. 3.5 to 3.8.

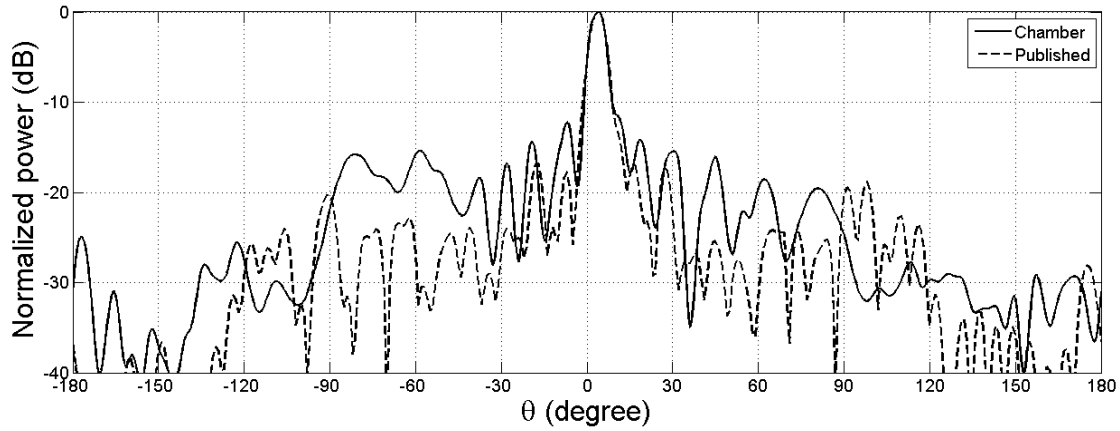


Fig. 3.5. Base station antenna far-field E-plane power patterns at 1.8 GHz.

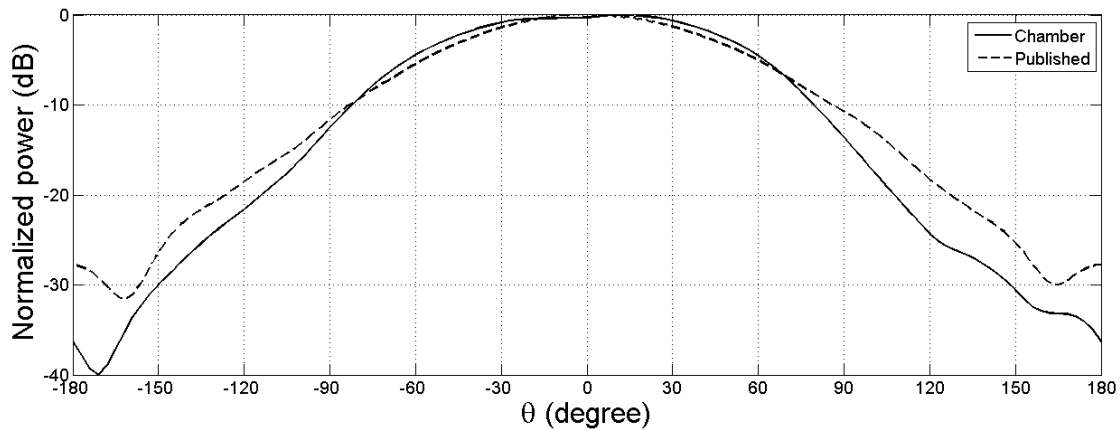


Fig. 3.6. Base station antenna far-field H-plane power patterns at 1.8 GHz.

From Figs. 3.3 to 3.8, we can see the agreements between the measured far-field patterns and the transformed far-field patterns are good at the main lobe in E-plane. Some deviations are observed at the first side lobes. This is probably because the antenna we measured is not the same specific unit from which the published far-fields data were

obtained. Thus we have the conclusion that antenna far-field patterns are successfully obtained by spherical near-field measurements and associated near-field to far-field transformations. The performance of our 6-inch circular waveguide probe is also validated. To be concrete, good far-field patterns fulfilled by only two sets of near-field measurement demonstrate the first-order property of the 6-inch probe.

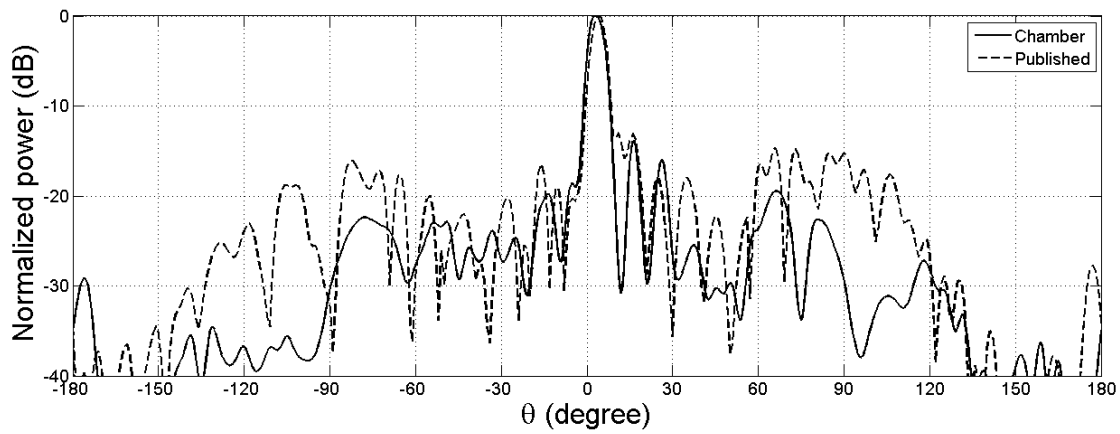


Fig. 3.7. Base station antenna far-field E-plane power patterns at 1.9 GHz.

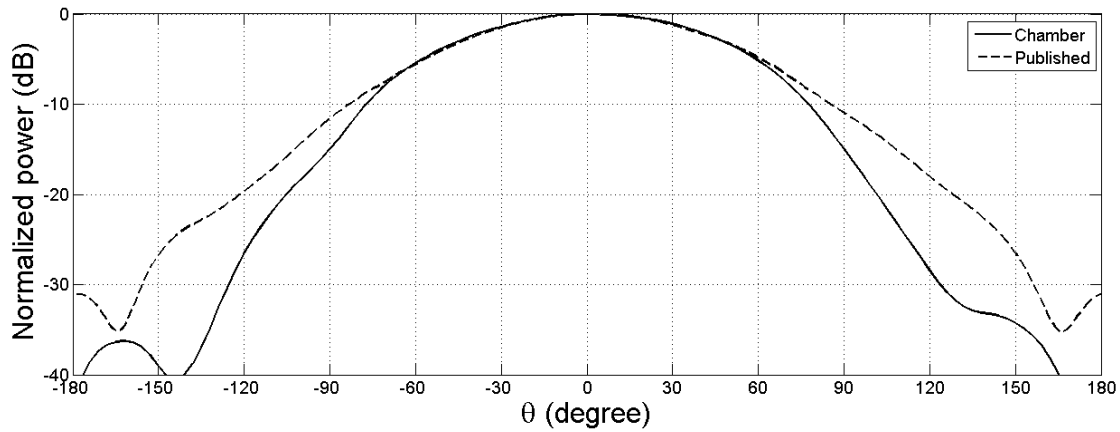


Fig. 3.8. Base station antenna far-field H-plane power patterns at 1.9 GHz.

## CHAPTER FOUR

### CONCLUSIONS

This thesis discusses new features of a circular waveguide probe applied to spherical near-field measurement. The first new feature is its short length, whose feasibility is supported by its demonstrated single-mode property. Second, the feeding scheme contributes to elimination of all the even modes, which is a new mechanism to control the modes besides the traditionally used cutoff method. This is essential to its operating frequency range extension. Lastly, the resonant cavity guarantees maximum radiated power of the probe at any frequency.

It is also shown that the first-order probe operation is not necessarily restricted to only  $TE_{11}$  mode. So long as the significant modes are all first-order modes like  $TE_{11}$  and  $TM_{11}$ , it is a first-order probe. This concept is also helpful in extending the probe's operating range. The first-order property of the probe was evidenced by its calibration measurements.

Finally, near-field measurements of a base station antenna were performed. The transformed far-field patterns show acceptable agreement with the measured far-field ones. Therefore, the usability of our first-order probe was validated.

## REFERENCES

- [1] J. E. Hansen, *Spherical Near-Field Antenna Measurements*. London, U.K.: Peter Peregrinus, 1988.
- [2] Wittmann, R. C., Stubenrauch, C. F., *Spherical-Near-Field Scanning: Experimental and Theoretical Studies*, National Institute of Standards and Technology (US), NISTIR 3955, 1990.
- [3] G. Engargiola and R. L. Plambeck, "Tests of a planar *L*-band orthomode transducer in circular waveguide," *Review of Science Instruments*, vol. 74, pp. 1380-1382, Mar. 2003.
- [4] R. E. Collin, *Field Theory of Guided Waves*. New York, NY, Wiley-Interscience, 1991.
- [5] R. E. Collin, *Foundations for Microwave Engineering*. New York, NY, Wiley-Interscience, 2001.
- [6] L. A. Weinstein, *The Theory of Diffraction and the Factorization Method*. Boulder, Colorado, The Golem Press, 1969.
- [7] A.V. Shishkova, S.N. Pivnenko, O.S. Kim and N.N. Gorobets, "Phase radiation characteristics of an open-ended," *IET Microw. Antennas Propag.*, 1, (3), pp. 790–797, 2007.